Int. J. Nano Dimens., 10 (1): 89-104, Winter 2019

ORIGINAL ARTICLE

Solid state synthesis of $MgAl_2O_4$ nanomaterials and solar light-induced photocatalytic removal of Malachite green

Sakineh Parvarinezhad, Mahdi Salehi, Shahin Kademinia*

Department of Chemistry, Semnan University, Semnan, Iran

Received 10 May 2018; revised 21 July 2018; accepted 03 August 2018; available online 04 August 2018

Abstract

Spinel $MgAl_2O_4$ nanopowders were synthesized by one-step solid state reactions using $Al(NO_3)_3.9H_2O$ and $MgSO_4$ raw materials at stoichiometric 1 : 2, Mg : Al molar ratio at a constant reaction temperature of 1000°C for 8 h (S_1), 10 h (S_2) and 24 h (S_3). The synthesized materials were characterized by powder X-ray diffraction (PXRD) technique. Structural analyses were performed by *FullProf* program making use of profile matching with constant scale factors. The results showed that the patterns had a cubic $MgAl_2O_4$ structure similar to the space group. Through textural analysis BJH (Barrette Joiner Halenda) and BET (Brunauer Emmett Teller) methods, the obtained materials were evaluated in terms of average pore size, specific surface area and average pore volume .The morphology of the obtained materials was studied by FESEM images. Ultraviolet–visible (UV-vis) spectra showed that the nanostructured $MgAl_2O_4$ powders possessed strong light absorption properties in the ultraviolet-visible region. Direct optical band gap energies were calculated as 3.4, 2.9 and 3.1 eV for S_1, S_2 and S_3, respectively. The photocatalytic performance of the synthesized nanomaterials was investigated for the degradation of pollutant Malachite Green (MG) in aqueous solutions under solar light. Optimum conditions (0.2 mL H_2O_2, 25 mg catalyst and 40 min catalytic reaction time for the removal of 80 mL of 100 ppm MG solution) were modeled and achieved by the design expert software for S_1. The degradation yield in the condition was 100 % for S_1.

Keywords: *Bandgap; Dye Degradation; Magnesium Aluminate Spinel; Malachite Green; Nano-Photocatalyst.*

How to cite this article

Parvarinezhad S, Salehi M, Kademinia S. Solid state synthesis of $MgAl_2O_4$ nanomaterials and solar light-induced photocatalytic removal of Malachite green. Int. J. Nano Dimens., 2019; 10 (1): 89-104.

INTRODUCTION

Magnesium aluminate spinel ($MgAl_2O_4$) is the most representative material belonging to the wide family of minerals with spinel crystalline structure. This material has a cubic crystal structure with the space group. O^{2-} anions are arranged in a close-packed pseudo-cubic sub lattice. Mg^{2+} ion occupies 1/8 of the available tetrahedron position. Moreover, 1/2 of the available octahedral sites, within the oxygen sub lattice, is occupied by Al^{3+} ions [1-2]. Magnesium aluminate is commonly utilized in metallurgical, radio technical and chemical industries owing to its desirable mechanical, chemical, and thermal properties. Magnesium aluminate synthesis has recently become more prominent using different methods such as solid state reactions via MgO and α-Al_2O_3, γ-Al_2O_3 and MgO , ρ-Al_2O_3 and MgO materials at 800, 1000, 1200, 1400 and 1600 °C [3], employing MgO and Al_2O_3 at 1500, 1650 °C [4], utilizing aluminum tri-hydroxide and caustic MgO at 1350 °C, 1-24h [5] ,Al_2O_3 and MgO at 1600 °C [6], $Al(NO_3)_3.9H_2O$, $Mg(NO_3)_2.6H_2O$ and CH_4N_2O and $MnCl_2.4H_2O$ at 500,1000 °C [7], $Mg(NO_3)_3$, $Al(NO_3)_3$ triethanolamine and HNO_3 at 650°, 675°, 700°, and 750 °C at a heating rate of 8–10°C/min. [8], MgO and Al_2O_3 at 400 and 600 °C [9], Solid state method [2], complexion of metal ions by chelating ligands and subsequent thermal treatments [10], coprecipitation of Mg and Al hydroxides [11], hydrothermal [12], sol-gel process [13], pyrolysis [14] and emulsion [15] methods. Due to its extreme thermal conductivity, high chemical stability and low dielectric constant

* Corresponding Author Email: *msalehi@semnan.ac.ir*

properties, there exist myriad applications for malachite green in the fields of photonics and metallurgy, and regarding ceramic, structural materials, electrical industry, support catalysts, moisture sensors and nuclear materials [16-19]. Furthermore, this material is widely employed in paint, leather, paper, cotton and silk industries. In the fishing industry specifically, it is used as an antifungal agent. Malachite Green, on the other hand, has many disadvantages; it is a non-digestible color contaminant material causing high levels of immune deficiency and reproduction in mosquitoes and aquatic animals. Inhaling and drinking MG is also hazardous, entailing eye and skin irritation. The main chemical structure of MG has metabolic symptoms in cancer formation. Experimental and clinical observations further indicate that MG is a toxic substance with regards to several organs and belongs to certain colorful groups of triphenylmethane, acting as a crystalline disruptor which leads to cancerous effects and diseases [20-21]. In the present study, a solid state method was explored for the synthesis of nanostructured $MgAl_2O_4$ powders using $MgSO_4$ and $Al(NO_3)_3.9H_2O$ raw materials. For the synthesis of the targets, thermal treatment conditions at 1000°C for 8 h, 10 h, and 24 h were investigated. The direct band gap energy of the obtained magnesium aluminate nanomaterial's were estimated from UV-Vis spectra. Further studied was the photocatalytic application of the synthesized magnesium aluminate for the degradation of MG under solar light. An experimental design method was used to optimize the factors influencing the dye removal reaction.

EXPERIMENTAL

General remarks

All chemicals were of analytical grade, obtained from commercial sources, and used without further purification. Phase identifications were performed on a powder X-ray diffractometer D5000 (Siemens AG, Munich, Germany) using CuK_α radiation. The morphologies of the obtained materials were examined with a field emission scanning electron microscope (Hitachi FE-SEM model S-4160). Absorption spectra were recorded on an Analytik Jena Specord 40 (Analytik Jena AG Analytical Instrumentation, Jena, Germany). Moreover, textural analysis was performed by Beckman Coulter SA3100 Surface Area Analyzer. The software used for designing the experiment (DOE) was Design Expert 7. The photocatalytic activity of the synthesized $MgAl_2O_4$ samples in the degradation of MG was measured in the presence of H_2O_2 (30%, w/w) under solar conditions.

Catalyst preparation

In a typical solid state synthesis experiment, 0.375 g (1 mmol) of $Al(NO_3).9H_2O$ (Mw = 375.0g mol^{-1}) and 0.0601 g (0.5 mmol) of $MgSO_4$ (Mw = 120.37 g mol^{-1}) were mixed and ground in a mortar until a nearly homogeneous powder was obtained. The obtained powder was added into a 25 mL crucible and treated thermally in an electrical furnace in a step at 1000 ºC for 8 h (S_1), 10 h (S_2), and 24 h (S_3). In the furnace, the crucible was allowed to be cooled normally to the room temperature. The obtained yellowish powder was collected for further analyses. The syntheses yields for $MgAl_2O_4$ (Mw=166 g mol^{-1}) were 72 % (S_1), 69 % (S_2), 68% (S_3). Using the design of the experiments, a photocatalytic activity was investigated in order to obtain an optimal value of 0.025 g of catalyst (S_1) and 0.2 mL of H_2O_2 in a 40 minute interval and is with using Malachite Green was obtained at a concentration of 100 ppm in a volume of 80 ml. 0.025 g of the catalyst to 80 ml of a solution containing 100 ppm malachite green was added, and glass containers containing the solution were covered with aluminum sheet to avoid exposure to sunlight. The resulting solution was then placed on a magnetic with magnetic stirrer at room temperature. After 10 minutes, 0.2 ml of H_2O_2 was added to it, and again exposed to light by removing the aluminum sheet and stirring for 40 minutes on a magnetic stirrer it placed. At the end, 15 ml of the resulting solution was centrifuged and the absorption spectrum was taken. As the absorption spectrum is observed, the optimum degradation mode is 100% also in Fig. 1 is seen. Photocatalysis activity, a photocrogen test was performed.

RESULTS AND DISCUSSIONS

Characterization

The crystal structure of the obtained nanomaterials was $MgAl_2O_4$, studied by Rietveld analysis using PXRD data. Fig. 2 (a-c) illustrates the analysis of the obtained PXRD data on a scale of 2θ to 10-90°. Structural analysis was performed by *FullProf* program to fit the profile with a constant scale factor. The red lines represent the observed intensities and the black lines are the calculated data; moreover, the blue lines

indicate the difference between the experimental and computational values. The results showed that the patterns corresponded to the cubic structure with a space group. There are three other phases in the mixture, including $MgSO_4$ [22], MgO [23], and α-Al_2O_3 [24]. At a reaction period of 8 h, the impurity phases conduce to the mixture for up to 49%.

The crystallite size of the nanomaterials synthesized at different reaction times were calculated by Scherrer equation (eq. 1) where D is crystallite size, $B_{1/2}$ is the width of the peak at half the maximum height (FWHM), λ is XRD wavelength (0.154 nm), K equals 0.9 and θ is the half of the angle at which the peak exists.

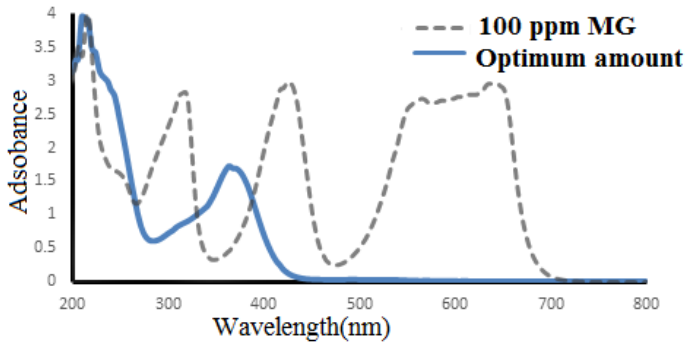

Fig. 1. The UV-Vis spectrum from Malachite Green with a concentration of 100 ppm and an optimum spectrum.

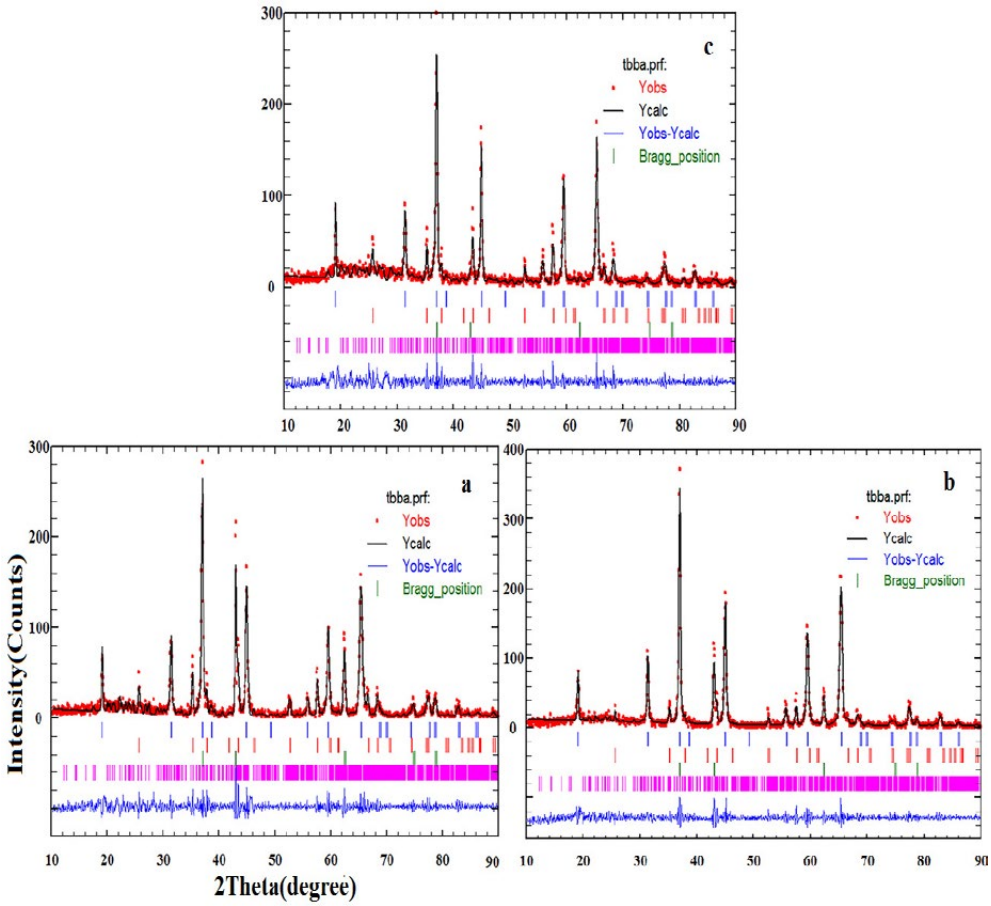

Fig. 2. PXRD patterns and the Rietveld analyses of a) S_1, b) S_2 and c) S_3.

$$cos\theta = \frac{K\lambda}{D} . \frac{1}{B_{\frac{1}{2}}} \quad (1)$$

Equation 1 was used to calculate the crystallite size of the samples. As it can be seen in Table 1, with the increase in the reaction time from 8 to 10 h the crystallites become larger; however, when the reaction goes past 24 h, no enlargement is observed in the crystallite size. Indicating that the effect of the reaction time on the crystallite size becomes significant once, it is increased up to 10 h.

The value of the dislocation density (δ), associated with the number of defects in the crystal, was calculated from the average values of the grain size (D) via the relationship given below:

$$\delta = \frac{1}{D^2} \quad (2)$$

Table 1 summarizes the dislocation values where the decrease in the dislocation density is due to the increase in the crystallite sizes of the materials resulted from the alteration in the reaction condition.

The strain (ε) values were also determined making use of the following formula:

$$\varepsilon = \frac{\beta_{hkl}\ cos\theta}{4} \quad (3)$$

Also included in Table 1 is the variation in the strain as a function of synthesis reaction conditions. The reduction in the strain values is probably due to the augment in the crystallite of the obtained crystals. It can therefore be inferred that synthesis reaction conditions influence the crystallite size, strain and dislocation density values**.**

Interplanar spacing data of the obtained nanomaterials were calculated by both Equations 4 and 5. In this regard, the peak with the highest intensity was employed in the range of 2θ = 36.98° for S_1, 2θ = 37.00° for S_2 and 2θ = 36.96° for S_3 with the miller indices (3 1 1).

$$n\lambda = 2d\ sin\vartheta \quad (4)$$

$$\frac{1}{d_{hkl}^2} = \frac{h^2 + k^2 + l^2}{a^2} \quad (5)$$

It can be seen that there exists a good agreement between the data obtained from Bragg Equations 4 and 5 where n=1, λ is the input wavelength of the X-ray, θ is the peak position and is lattice parameter.

Table 2 shows the lattice parameter data of S_1 to S_3. The lattice parameter *a* of the $MgAl_2O_4$ samples shows that at a constant reaction temperature, there is no considerable change in the unit cell volume. R_F, R_{Bragg} and χ^2 of the syntheses show that the analyses were good because R_F, R_{Bragg} analysis is less than 5 and χ^2 less than 2 is acceptable. Besides, the purity data indicated that increasing the reaction time enhanced the crystalline purity of the targets. However, it is clear that increasing the reaction time to 24 h entails no significant effect on the crystal phase purity of the synthesized material.

FT-IR spectra

FT-IR spectra of the as-synthesized powders confirm that dehydration occurs during the thermal treatment (Fig. 2a, b and c). Release of water molecules from the defect structure of hydroxides and their consecutive adsorption on the surface of dehydrated products are documented by the fact that the peaks at wave

Table 1. Crystallite size data obtained from Scherrer equation.

Sample	2θ	Θ	$\beta_{1/2}$ (°)	$\beta_{1/2}$ (rad)	$\cos\theta_\beta$	D(nm)	δ(lines/m^2) × 10^{14}	ε
S_1	36.9822	18.4645	0.34186	0.005963	0/9485	24	0.00173	0.00141
S_2	37.0021	18.5010	0.30254	0.005277	0/9398	28	0.00127	0.00124
S_3	36.9646	18.4823	0.30222	0.005277	0.9333	28	0.00127	0.00123

Table 2. Lattice parameter, interplanar spacing, rietveld and purity data for the obtained nanomaterials.

Sample	a=b=c (Å)	d_{Bragg} (Å)	$d_{cal.}$	R_{Bragg}	R_F	χ^2	Purity (%)
S_1	8.066	2.431	2.432	0.661	0.401	1.46	51
S_2	8.068	2.432	2.432	0.832	0.82	1.65	66
S_3	8.075	2.434	2.434	1.37	1.04	1.572	70

numbers 3510, 343, and 3370 cm^{-1} merge into one broad band with a maximum at 3400 cm^{-1} (the valence vibration of water). Results of FT-IR spectroscopy displayed that the band with a maximum at 800 cm^{-1} becomes more emphasized with increasing reaction time from 8 h to 24 h (Fig. 3b and c), which splits into two bands at 560 and 700 cm^{-1} at 1000C. These bands are characteristic for vibration Mg-O and Al-O groups of the spinel structure (Fig. 3b, c). [25].

Morphology analysis

Fig. 4 (a-d) shows the FESEM images of $MgAl_2O_4$ powder synthesized at 1000 °C for 8 h. Fig. 4 (a, b) demonstrates that there is a porous morphology in the image and Fig. 4 (c, d) shows that the material is composed of particles. Fig. 5 shows the particle size distribution profile of the synthesized $MgAl_2O_4$ particles. Where, the maximum particle size distribution falls in the range of 30-50 nm.

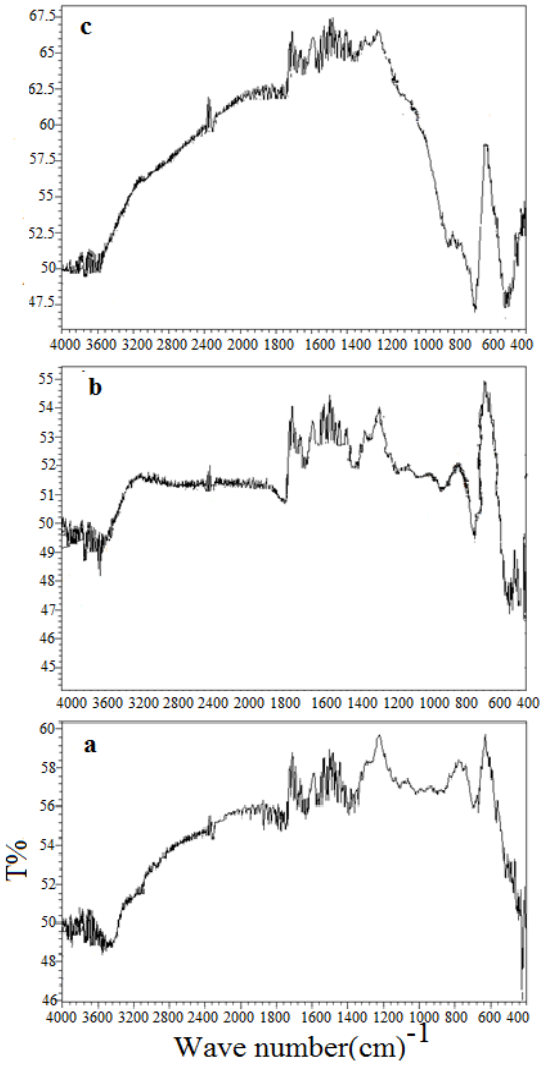

Fig. 3. FT-IR spectrum of a) S_1, b) S_2 and c) S_3.

Fig. 6 (a,b) shows the FESEM images of $MgAl_2O_4$ sample synthesized at 1000 °C for 10 hours (S_2). As observed, the morphology is changed with the increase in the reaction time and the materials are composed of agglomerated particles forming a porous morphology. The diameter of the components is about 50-60 nm, which is larger than S_1.

Fig. 7 (a-d) shows the FESEM images of $MgAl_2O_4$ synthesized at 1000 °C for 24 hours (S_3). Fig. 7 (a, b) shows that when the reaction time is increased, the morphology changes into sponge. Fig. 7 (c, d) indicates that the sponge structure is highly homogeneous and the particles are arranged in a way that leads to the formation of a high ordered sponge morphology. Furthermore, the distribution of the particle size is homogeneous. Fig. 8 demonstrates the statistical results of the particle size distribution profile of S_3 where. The average particle size is in the range of 20-50 nm.

Textural Analysis

The obtained powders were studied using BJH and BET methods for surface area, average particle, average volume, mean porosity and average pore volume. Prior to N_2-physical adsorption measurement, the samples were degassed at 150 °C for 120 min in the nitrogen atmosphere. Accordingly, the specific surface area (S_{BET}) of the obtained materials was determined with adsorption-desorption isotherms of N_2 at 77 K. In addition, the specific surface area (S_{BET}) of the synthesized samples was determined by adsorption-desorption isotherms of N_2 gas at a temperature of 77 K. Table 3 shows the information obtained from the BET analysis, including surface area, pore volume, mean pore diameter, total pore volume, and the average diameter of the pore.

The surface areas and average pore diameters of S_1, S_2 and S_3 are about 25 (m^2/g), 20 (m^2/g) and 18 (m^2/g) and 24 nm, 29 nm and 26 nm, respectively. The data show that pore volume decreases with the increase in the reaction time from 8 h to 24 h, hence the fact that the pore volume and surface area are inversely related to the reaction time, yet directly associated with the purity and the crystallite size of the targets.

Table 4 summarizes the information obtained

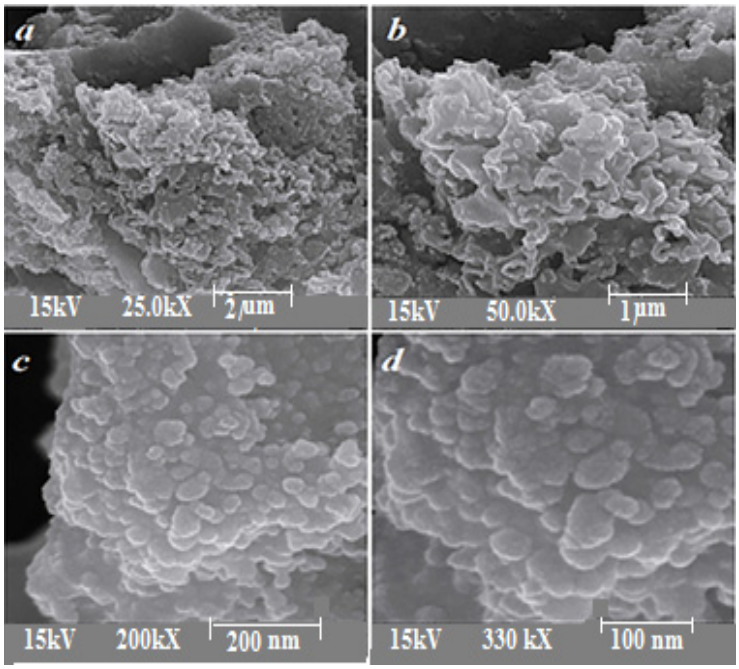

Fig. 4. FESEM images of S_1.

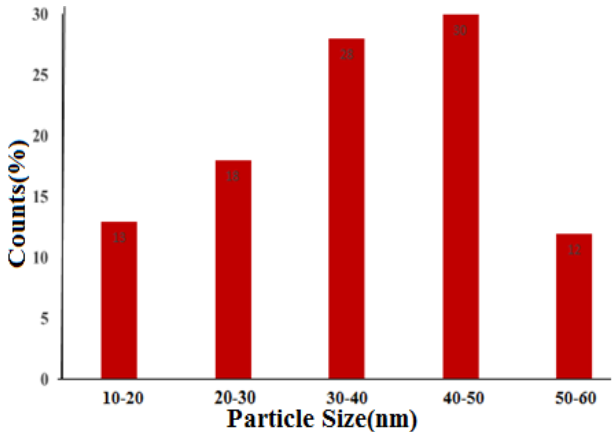

Fig. 5. Particle size distribution profile of S_1.

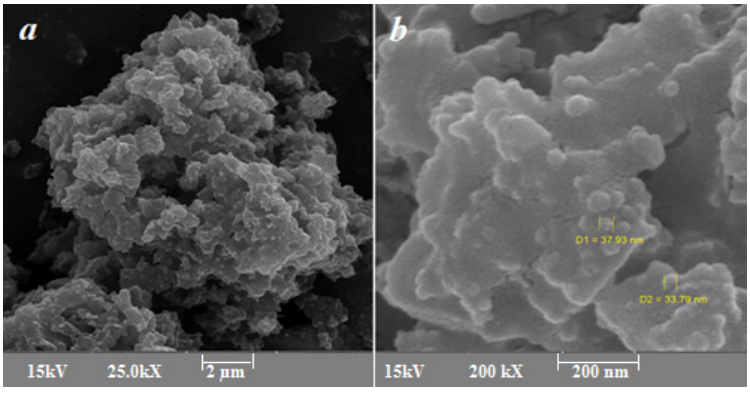

Fig. 6. FESEM images of S_2.

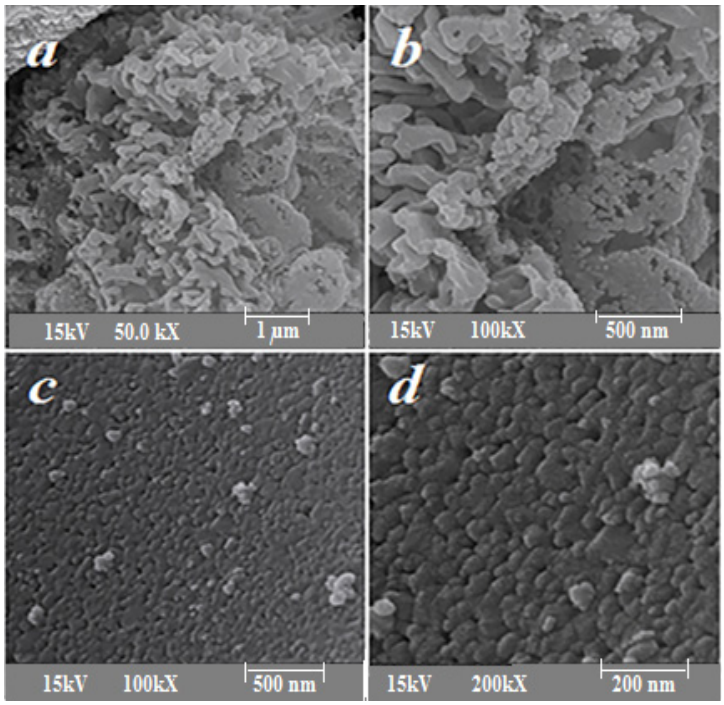

Fig. 7. FESEM images of S_3.

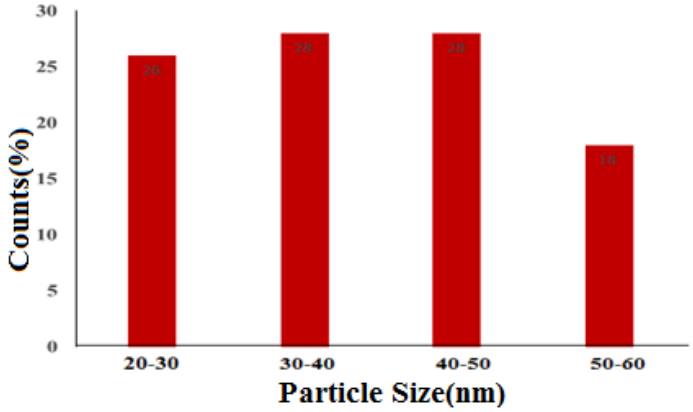

Fig. 8. Particle size distribution profile results of S_3.

Table 3. BET textural data of the Spinel $MgAl_2O_4$ samples.

Sample	Total pore volume	pore volume (cm^3/g)	Area (m^2/g)	Diameter (nm)
S_1	0.1514	5.80	25	24
S_2	0.1447	4.56	20	29
S_3	0.1171	4.20	18	26

Table 4 .BJH textural data of the Spinel $MgAl_2O_4$ sample.

Sample	surface area (m^2/g)	Pore volume (cm^3/g)	4V/a	Width (nm)
S_1	29.409	0.1543	2.09	9.21
S_2	21.847	0.1462	2.67	7.98
S_3	20.674	0.1189	2.30	7.98

from the BJH analysis of the synthesized nanomaterials regarding pore surface area, pore volume and the average particle size of the targets. The results of BET and BJH measurements show that the pore surface area and volume of S_1 are larger than those of S_2 and S_3.

Optical properties

Fig. 7 shows the UV-Vis spectra and direct band gap energies of $MgAl_2O_4$ nanomaterials calculated from the UV-Vis spectra. The synthesized $MgAl_2O_4$ band gap energies were calculated by an equation introduced by Pascual *et al.* [19]. There is a relation between the absorption coefficient and the energy of the incident photon, $(ah\nu)^2$ = A ($h\nu$-Eg) where Eg is the band gap energy by extrapolating the linear part of the curve to the energy axis [26]. Fig. 9 a shows UV-vis spectrum S_1 where the wavelength of the absorption edge is approximately 277 nm. Fig. 9 b indicates the direct optical band gap energy diagram of S_1 where Eg values are 3.45 and 5.12 eV. Fig. 9 (c, d) shows the UV-vis spectrum and optical band gap energy diagrams of S_2 in which the Eg values are 2.9 and 4 eV. In fact, the reduction in the band gap value indicates the increase of the crystalline size of the nanomaterials. Fig. 9 (e, f) shows the UV-Vis spectrum and the optical band gap energy diagrams of S_3. Fig. 9 f demonstrates that the Eg value is about 3.1 and 4 eV.

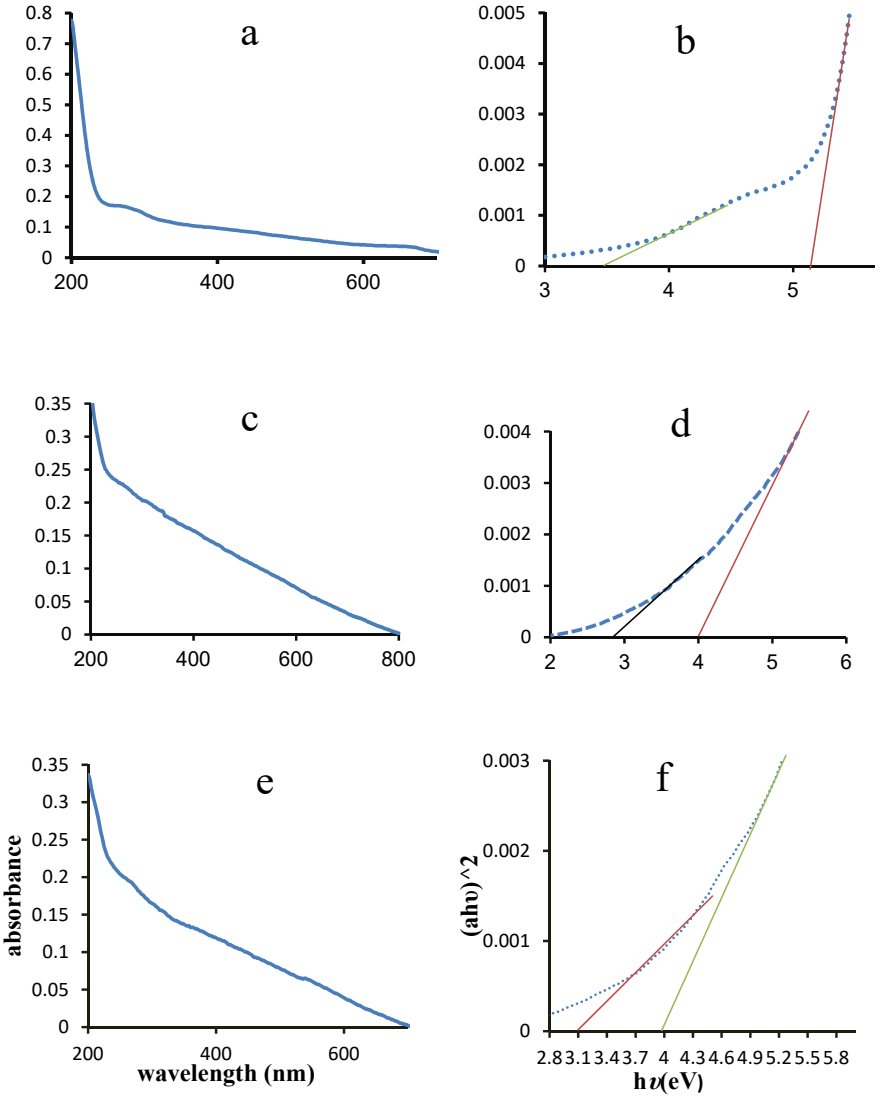

Fig. 9. Plots of (a, c, e) UV-Vis spectrum, (b, d, f) $(\alpha h\upsilon)^2$ versus hυ for S_1, S_2 and S_3, respectively.

Photocatalytic activity

The photocatalytic activity of the synthesized samples was investigated for the degradation of MG in the presence of H_2O_2 (30%, w/w) under solar light. To prepare 100 ppm MG solution, 8 mg of MG powder was dissolved in 80 mL of deionized water. The pH value of the obtained solution was 4. In a typical photocatalytic experiment, a certain amount of S_1 was added to 80 mL of the prepared MG aqueous solution and sonicated for 10 min in a dark room to establish an adsorption/desorption equilibrium between MG molecules and the surface of the photocatalyst. Afterwards, certain volume of H_2O_2 was added into the mixture, followed by further magnetic stirring under solar light. With the passage of the considered time, the solution is drawn out and the photocatalyst is separated by centrifugation in order to measure the absorption spectra of MG and calculate the MG concentration using UV-Vis spectrophotometry. The mixture is further maintained at a constant stirring of 300 rpm at experiment temperature. The photodegradation yield (%) of MG was calculated via the following formula:

$$\left(\frac{A_0\text{-}A_t}{A_0}\right) \times 100 \quad (6)$$

Where, A_0 and A_t represent the initial absorbance of MG at 612 nm and the absorbance at time t, respectively.

Experimental design for achieving optimal conditions in MG degradation process

The optimal conditions were obtained by design expert software for S_1. It was found that the optimum condition was 0.2 mL H_2O_2, 25 mg catalyst and 40 min catalytic reaction time for the removal of 80 mL of 100 ppm MG solution. In a full factorial method, the association between factors and response is theoretically modeled enabling the reproducibility in the phenomenon under study to experiment with it and elucidate the results. Response surface methodology (RSM) is a mathematical and statistical method which analyzes experimental design by applying an empirical model. The adequacy of the applied model is checked through the use of analysis of variance (ANOVA) which requires certain replicate experiments. In the present study, the objective was to determine the amount of nanocatalyst and the time and H_2O_2 volume at which the degradation is to be monitored; the response was the obtained degradation (%). Different possible combinations of such factors were designed and reported in Table 5. All experiments were randomly done over two days. The central composite design (CCD) was selected for modelling and optimizing the proposed procedure based on S_1. A three-level CCD with three factors (H_2O_2 (A) catalyst (B) and time (C)) was employed to investigate the effects of the factors. Table 5 further illustrates the conditions of 20 experiments designed by CCD along with dye degradation percentage (response (R %)). The experimental range and levels of independent variables are given in Table 6.

As shown in Table 7, coded forms (-α, -1, 0, +1, +α) were assigned to independent variables (H_2O_2 volume (A_1), catalyst amount (A_2) and stirring time (A_3)).

The observed data of the factorial design was fitted to a linear response model. Prior to the

Table 5. Three-level full factorial design in photodegradation process.

Day	H_2O_2 (mL)	Catalyst (g)	Time (min)	Yield (%)
Day 1	0.2	0.01	40	60
Day 1	0.1	0.01	40	5
Day 1	0.15	0.0175	30	18
Day 1	0.1	0.01	20	15
Day 1	0.2	0.025	20	14
Day 1	0.2	0.01	20	15
Day 1	0.15	0.0175	30	17
Day 1	0.1	0.025	40	81
Day 1	0.15	0.0175	30	17
Day 1	0.1	0.025	20	50
Day 1	0.15	0.0175	30	15
Day 1	0.2	0.025	40	100
Day 2	0.066	0.0175	30	10
Day 2	0.15	0.030	30	90
Day 2	0.23	0.0175	30	26
Day 2	0.15	0.005	30	17
Day 2	0.15	0.0175	30	16
Day 2	0.15	0.0175	13	10
Day 2	0.15	0.0175	30	14
Day 2	0.15	0.0175	47	68

analysis, low and high factor levels were coded to -1 and +1, respectively (Table 7). The equation below shows the relationship between the factors and reaction yield, Y%, based on the first order model:

$$\%Y=15/5+\ 4/75\times H_2O_2\ +\ 19/97\times Catalyst\ +\ 18/27\ \times Time\ -\ 9\times Catalyst\times H_2O_2\ +\ 13/75H_2O_2\times time\ +\ 10/25catalyst.time+1/63\times\ (H_2O_2)^2\ 9/06\times\ (time)^2\ +14\ /18\ (catalyst)^2 \quad (7)$$

The quality of the model was statistically evaluated by the analysis of variance (ANOVA) and standard least squares techniques (Table 7), These analyses both comparing the differences between the averages of a group with the variability within the groups around the corresponding average values, a ratio called F-distribution (F-value), varying from 1 to larger amounts. Values far from 1, exceeding from the tabulated F-value, provide evidence against the null hypothesis, indicating the significance of the regression parts of the fitted models. Equivalently, the null hypothesis is rejected when p-value is less than a significant level. In order to obtain a reliable model at a 95% confidence level, the p-values of the fitted model and its corresponding terms have to be lower than 0.05. The p-value of the present regression was smaller than 0.05, showing that the model was reliable with a high confidence level (95%). The fitted model can be further assessed using the lack-of-fit test through which, the residual part is sub-divided into pure error and lack-of-fit. In other words, it distinguishes the random error from the systematic one, causing the lack of fitting of the models with specific orders. Therefore, at 95% confidence level, the p-values for the lack-of-fits are to be greater than 0.05, which is not significant. As shown in Table 7, the outcomes of ANOVA are entirely in agreement with the above statements.

To illustrate the effects in the foregoing model, the three–dimensional (3D) response surface plots of the responses (using equation (6) when the amount of time was fixed at an optimal level and the other two parameters were allowed to vary) are included in Fig. 8. Response surface methodology (RSM) was used to investigate the interactive effects of the three influential factors on the proposed process. Fig. 8 illustrates the 3D plots related to the interaction of AB (Fig. 10.a), AC (Fig. 10.b) and BC (Fig. 10.c). The semi-curvatures of these plots indicate the interaction between the variables. In other words, MG removal percentage is improved when the reaction time, H_2O_2 volume and catalyst amount are augmented, meaning that the mass transfer of dye molecules is enhanced on the surface of the catalyst. Furthermore, by increasing the catalyst amount, more adsorbent surface area becomes available for dye molecules, increasing the dye removal percentage.

The coefficient of determination (the R-square,

Table 6. The experimental range and levels of independent variables in CCD.

Factor	Low Actual	High Actual	Low Coded	High Coded	Mean
H_2O_2 (A)	0/066	0.23	-1	1	0.148
Catalyst(B)	4.8	30	-1	1	17.4
Time (C)	13.18	46.8	-1	1	29.99

Table 7. Analysis of variance for suggested model.

Source	Squares	Df	Square	Value	Prob >f	
Block	31.008333	1	31.00833			
Model	17068.948	9	1896.55	329.2378	< 0.0001	significant
A-H_2O_2	308.49985	1	308.4998	53.55505	< 0.0001	
B-Catalyst	5448.1032	1	5448.103	945.7815	< 0.0001	
C-Time	4559.7763	1	4559.776	791.5694	< 0.0001	
AB	648	1	648	112.4917	< 0.0001	
AC	1512.5	1	1512.5	262.5674	< 0.0001	
BC	840.5	1	840.5	145.9094	< 0.0001	
A^2	38.575303	1	38.5753	6.696607	0.0293	
B^2	2898.6541	1	2898.654	503.2014	< 0.0001	
C^2	1182.3529	1	1182.353	205.2545	< 0.0001	
Residual	51.843825	9	5.760425			
Lack of Fit	45.093825	5	9.018765	5.344453	0.0647	
Pure Error	6.75	4	1.6875			
Cor Total	17151.8	19				

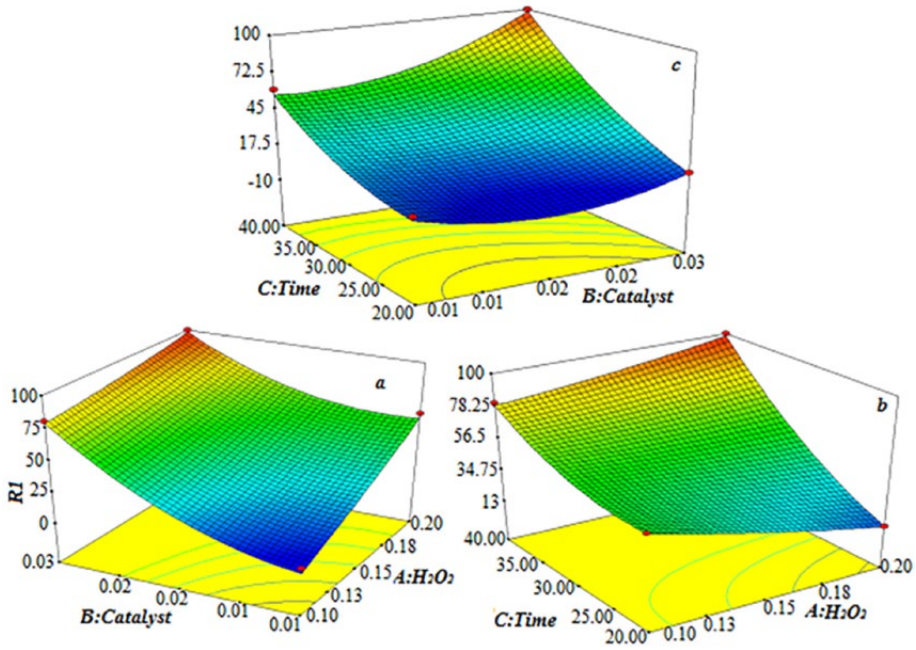

Fig. 10. 3D surface plot of removal of MG dye.

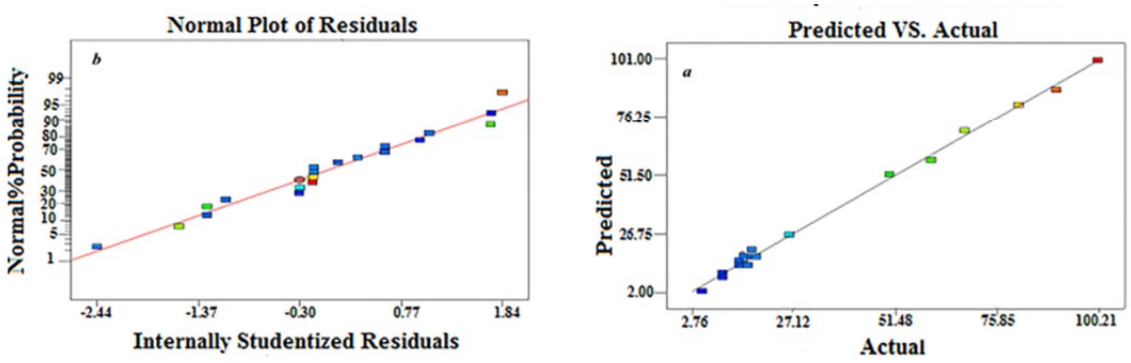

Fig. 11. (a) Experimental data versus the predicted data of normalized removal of dye and (b) normalized residual plot.

adjusted–R-square) was further made use of to express the quality of fit related to the polynomial model equation, where R^2 of variation fitting Y% = 100 indicates a high degree of correlation between the response and the independent factors (R^2 = 0.9969). Also, a high adjusted regression coefficient (R^2-adj = 0.9939) implies that the proposed model is greatly significant, meaning the difference between experimental and the predicted responses is negligible. The predicted R-squared value (0.97) indicates the high accuracy and reliability of the developed mode in the determination of the response value, demonstrated in Fig. 11(a, b).

The photocatalytic activity of commercially available titanium dioxide powder was investigated for comparison with similar conditions [27]. Fig. 12 (a-d) shows an MG removal study of the obtained nanomaterials. Specifically, Fig. 12 a indicates the effect of MG concentration on the degradation of MG where it is clear that by increasing MG concentration up to 150 ppm, the dye removal is reduced; moreover, by increasing MG concentration up to 120 ppm, the dye removal is reduced. It seems that when MG concentration is high, the light wavelength cannot penetrate the solution and the photocatalytic reaction is not carried out efficiently. Fig. 12 b shows the effect

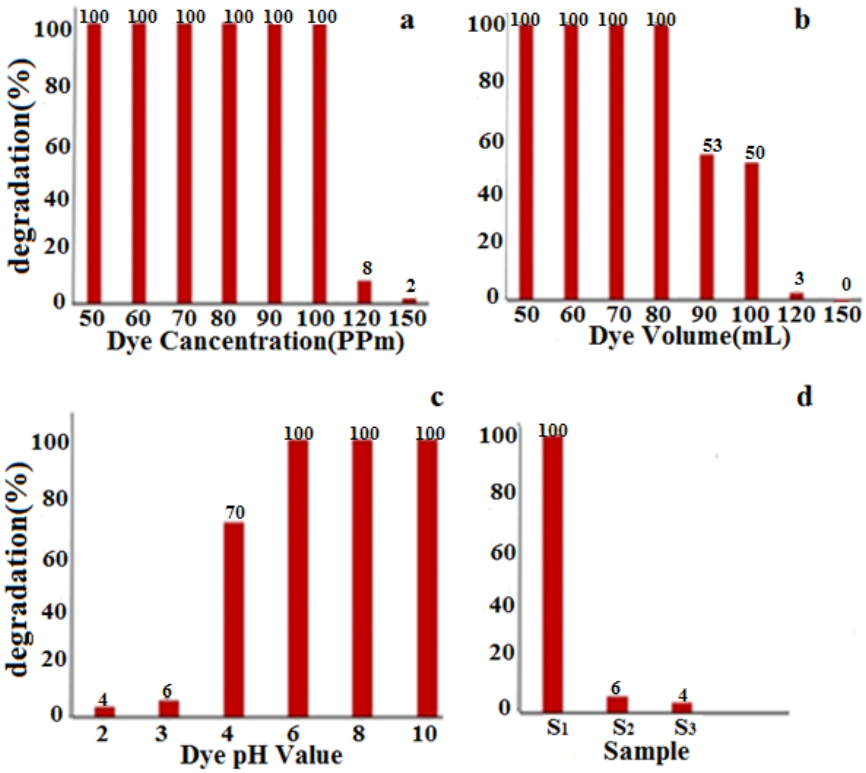

Fig. 12. MG degradation yields at (a) different dye concentrations, (b) different dye volumes, (c) different dye pH values, (d) comparison tests of S_1 to S_3.

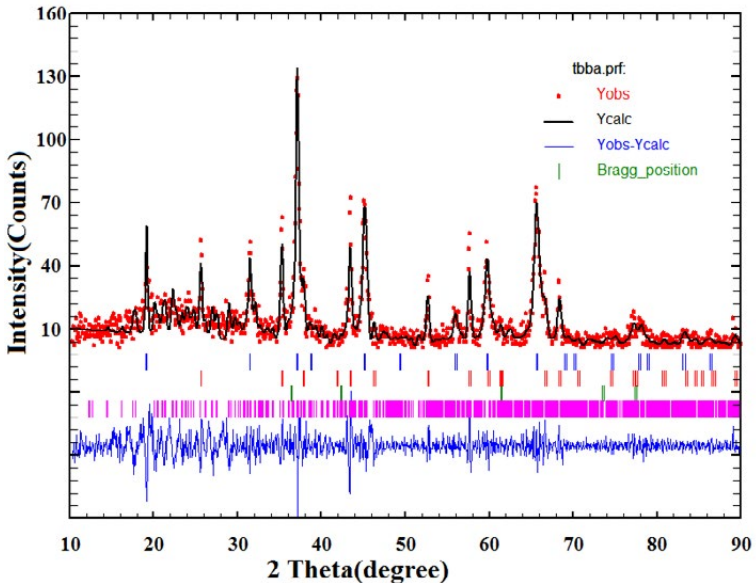

Fig. 13. Rietveld analysis and PXRD pattern of S_1 after photocatalytic application.

of MG volume on the degree of color removal. As observed, the dye removal yield is 100% when the volume is 50, 60, 70 or 80 mL. At 90, 100, 120, and 150 mL, the degradation yield is reduced owing to the reduction in the dye removal photocatalytic process. Fig. 12 c shows the effect of pH on the degree of color degradation. The pH of a neutral solution of MG is around 4. At a pH of 2-3, the MG

removal yield is low, while by increasing this factor from 4 to 10. OH concentration is increased in the solution speeding the process and augmenting the yield [28]. Fig. 12 d compares the influences of synthesized nanomaterials on MG removal yield. The data show that when the catalyst size is increased, the degradation is reduced. Hence, it can be concluded that catalyst particle size is a very important factor for MG removal photocatalytic application. In another study on the effects of raw materials on dye removal yields, it was found that the MG removal yield was reduced when the synthesis reaction time was increased from 10 h to 24 h which is due to the more composite nature effect of S_1 compared to S_2 and S_3.

Photo corrosion study was performed to investigate the photo chemical stability of S_1 in the photocatalytic process. Following the use of a catalyst in the photocatalytic application under optimum conditions, the catalyst was separated by filtration and investigated via PXRD technique. Fig. 13 shows the Rietveld analysis of the sample where the catalyst is not destroyed in MG photocatalytic removal process.

Table 8 represents the crystallite size data obtained from S_1 following use in the photocatalytic reaction. The crystallite size was calculated using Scherer equation with the peak positioned at 2θ = 37.033 for S_1 sample. As can be seen in Table 8, the catalyst is not destroyed when employed in the photocatalytic process.

Table 9 shows the crystallographic data of the catalyst after using in the photocatalytic process. As shown in the table, with the change in the cell parameter, no significant change occurs in photocatalysis activity and photo corrosion study. R_F factor, R_{Bragg} and χ^2 of the syntheses show that the analysis is good.

Mechanism for the photocatalytic process

The mechanism of converting solar energy to chemical energy in the photocatalysis by $MgAl_2O_4$ could be similar to previously reported and extensively studied mechanism; in a way that electrons (e^-) and holes (h^+) could be excited under visible irradiation to the conduction band and the valence band edge, respectively. These photo-excited e^- and h^+ then can transfer to the surface of the photocatalyst ($MgAl_2O_4$ particles), where they react with oxidants and reductants, respectively, or recombine in the absence of e^- and h^+ traps. The recombination of e^- and h^+ could be greatly minimized in the presence of H_2O_2, which traps the e^- and h^+ to form $^{\bullet}OH$ and $^{\bullet}O_2^-$ species [29]. The excited e^- reacts with H_2O_2 to form $HO^{\bullet}$ and OH^- groups. The formed OH^- group reacts with h^+ and forms $HO^{\bullet}$ group. Besides, H_2O_2 can trap the photoexcited species in another way. It reacts with h^+ and forms $HO_2^{\bullet}$ radical and H^+. The produced $HO_2^{\bullet}$ is decomposed to $^{\bullet}O_2^-$ and H^+. H_2O as the solvent of the photodegradation reaction can react with h^+ to form $HO^{\bullet}$ and H^+ species. The produced H^+ ion reacts with the dissolved O_2 and $2e^-$ and forms the initial H_2O_2. The dissolved O_2 can also react with e^- to form $^{\bullet}O_2^-$. The so-formed $^{\bullet}OH$ or $^{\bullet}O_2^-$ species are used for the decomposition of organic contamination molecules such as MG to intermediates or mineralized products through oxidation reactions [30-32].

$$MgAl_2O_4 + h\nu \rightarrow h^+ (MgAl_2O_4) + e^- (MgAl_2O_4) \quad (8)$$

$$H_2O_2 + e^- (MgAl_2O_4) \rightarrow HO^{\bullet} + OH^- \quad (9)$$

$$OH^- + h^+ (MgAl_2O_4) \rightarrow HO^{\bullet} \quad (10)$$

$$H_2O_2 + h^+ (MgAl_2O_4) \rightarrow HO_2^{\bullet} + H^+ \quad (11)$$

$$HO_2^{\bullet} \rightarrow \bullet O_2^- + H^+ \quad (12)$$

$$H_2O + h^+ (MgAl_2O_4) \rightarrow HO^{\bullet} + H^+ \quad (13)$$

$$2H^+ + O_2 + 2e^- \rightarrow H_2O_2 \quad (14)$$

$$O_2 + e^- (MgAl_2O_4) \rightarrow \bullet O_2^- \quad (15)$$

$$MG + OH^{\bullet} + \bullet O_2^- \rightarrow \text{degradation product} \quad (16)$$

The maximum removal efficiency (100 %) was

Table 8. Crystallite size data obtained from Scherer equation after using in the photocatalytic application.

Sample	2θ	θ	$B_{1/2}$ (°)	$B_{1/2}$ (rad)	Cosθ	D (nm)
S_1	37.033	18.5156	0.34196	0.005965	0.9502	24

Table 9. Cell parameters and rietveld analysis data of S_1.

Sample	a=b=c (Å)	R_{Bragg}	R_F	χ^2
S_1	8.046	1.49	0.79	1.86

Table 10. Comparison study of the photocatalytic ability of the synthesized $MgAl_2O_4$ with other catalysts.

	Catalyst	Condition	Yield (%)	Ref
1	$MgAl_2O_4$	H_2O_2, 25 mg catalyst, 40 min, Solar ligth, 80 mL of 100 ppm MG	100	Present work
2	TiO_2	UV irradiation, 4 h, 500 ppm catalyst, 50 ppm MG	100	[21]
3	Carbon/TiO_2	25 ppm MG, 30 min, pH=8	82-100	[34]
4	MoS_2/TiO_2	40 min, sunlight irradiation, 0.1 g catalyst, 10 ppm MG	97	[35]
5	$PbCrO_4$	365 ppm MG, 0.1 g catalyst, 4 h, pH=7.5, visible light, 60 min	90	[36]
6	TiO_2/ZnO	UV light, pH=7, 50 ppm MG, 1.5 g/L catalyst	100	[37]
7	Nix:TiO_2	25 mL of 10 µM MG, UV light	90	[38]
8	TiO_2	UV Light, 1 h, 20 mg catalyst, 40 ppm MG	100	[39]
9	V doped-ZnO	UV and visible lights, 500 ppm MG, 500 ppm catalyst, 200 min	90	[40]
10	$Ni_{1-x}Co_xFe_2O_4$	Sunlight, 50 mL of 25 ppm catalyst, 1 µM MG, H_2O_2, 15 h	100	[41]
11	Pt/TiO_2/SiO_2	UV and visible lights, 60 min	80	[42]
12	Fe^{3+} doped TiO_2	UV and visible lights, 5 ppm MG	85	[43]
13	$FeVO_4$	0.03 g catalyst, UV light, 300 min	90	[44]
14	La/N co-doped TiO_2	50 W tungsten halogen lamp, 500 mL of 30 ppm MG, 240 min	100	[45]
15	UV/H_2O_2	UV lamp (30 W, UV-C), 200 ml MG, 10 ppm, 2 h	100	[46]
16	$Cd(OH)_2$-NW-AC	0.06 g catalyst, 50 mL of 15 ppm MG, 35 min	90	[47]
17	ZnO-NP-AC	50 mL of 15 ppm MG, 0.015 g catalyst, 35min, pH=7	95	[48]
18	S-Me/MA	6 mL of 1000 ppm MG, 50 °C, 24 h, 0.06 g catalyst, pH=10	98	[49]
19	Fe_3O_4@Mel	0.3 g catalyst, pH=6.3, 100 mL of 8 ppm MG, 20 min	$9mg_{MG}/g_{cat}$	[50]
20	TiO_2/WO_3	pH=12, UV light, 1000 ppm catalyst, 30 min	97	[51]
21	$FeSO_4$ -7H_2O	10 mM Fe^{2+}, 40 °C, 25.5 mM H_2O_2, 10 ppm MG	94	[52]
22	TiO_2-Co_2O_3	1 ppm MG, using 125 W mercury lamp, 60 min	93	[53]
23	SnO_2-CuO	UV light, 20 ppm MG, 0.1 g catalyst, 180 min	96	[54]
24	Mg-doped TiO_2	Vis light, pH=9, 100 ppm MG	89	[55]
25	ZnO	4h time, 60 ppm MG, pH=7.5, solar radiation	98	[56]
26	Prosopis cineraria	100 mL of 500 ppm MG, 0.4 g PCSD, 3 h	80	[57]
27	Polyoxometalates	0.1 g catalyst, 200 mL of 0.02 mM of MG, 160 min	65	[58]
28	$Zn_xFe_{3-x}O_4$	UV light, 1 g catalyst, 10 µM MG	90	[59]
29	Ni/$MgFe_2O_4$	50 mL of 0.8 g/L MG, 30 mg of catalyst, UV light, pH=4	93	[60]
30	$Sr_2As_2O_7$	H_2O_2, 20 mg catalyst, 33 min, 70 mL of 100 ppm MG, solar light	97	[61]

obtained at 0.2 mL of H_2O_2 volume, and it slightly decreased above the volume. It is because the produced highly reactive hydroxyl radical (eq. 18) reacts with excess amount of H_2O_2 and produces hydroperoxyl radical ($HO_2^{\bullet}$) (eq. 19) which is less reactive and ultimately inhibits the degradation with producing O_2 and H_2O in (eq. 21). The reaction mechanism is explained below [32, 33]:

$$H_2O_2 + e^- (MgAl_2O_4) \rightarrow HO^{\bullet} + OH^- \quad (17)$$

$$OH^- + h^+ (MgAl_2O_4) \rightarrow HO^{\bullet} \quad (18)$$

$$H_2O_2 + HO^{\bullet} \rightarrow HO_2^{\bullet} + H_2O \quad (19)$$

$$H_2O_2 + HO_2^{\bullet} \rightarrow HO^{\bullet} + O_2 + H_2O \quad (20)$$

$$HO^{\bullet} + HO_2^{\bullet} \rightarrow O_2 + H_2O \quad (21)$$

To illustrate the merit of the present work, we compared the results of the as-prepared $MgAl_2O_4$ nanocatalyst with some of the catalysts reported for MG degradation. Table 10 shows the results of the reported catalysts to remove MG. It is clear that synthesized $MgAl_2O_4$ has more catalytic activity compared to other heterogeneous catalysts.

CONCLUSION

This study explored and described the synthesis of solid state crystalline nanoscale magnesium aluminate materials. XRD patterns represented the synthesis of magnesium aluminate crystals under solid state conditions. Rietveld analysis showed that reaction time played an important role in the crystal growth of the obtained materials. It was further observed that reaction time is an important factor concerning crystal size and the degree of purity of the obtained material. The crystal phase purity augments with increase in the reaction time. In addition, the morphology of the nanomaterials undergoes no change, yet the particle size increases by raising the reaction time. The data showed that the obtained nanomaterial efficiently removes MG contaminants in aqueous solution. Results obtained from the design expert software showed that the optimum condition (under which malachite green is entirely removed) is 25 mg of catalysts and 0.2 mL of hydrogen peroxide with MG concentration of 100 ppm and MG volume of 80 mL over a 40 min time period. At pH values of more than 4, the degradation process increases. High degradation yields can be further achieved at MG concentrations less than 100 ppm

and MG volumes less than 80 mL. According to the photo corrosion experiment, the catalyst was not degraded following the photocatalysis process.

ACKNOWLEGMENTS

The authors declare their sincere thank from Semnan University for supporting the present study.

CONFLICT OF INTEREST

The authors declare that there is no conflict of interests regarding the publication of this review article.

REFERENCES

[1] Sickafus K. E., Will J. M., (1999), Structure of Spinel. *J. Am. Ceram. Soc*. 82: 3279- 3292.

[2] Ball J. A., Murphy S. T., Grimes R. W., Bacorisen D., Smith R., Uberuaga B. P., Sickafus K. E., (2008), Defect processes in $MgAl_2O_4$ spinel. *Solid State Sci*. 10: 717-722.

[3] Zhang Zh., Nan Li., (2005), Effect of polymorphism of Al_2O_3 on the synthesis of magnesium aluminate spinel. *Ceram. Int*. 31(b): 583-589.

[4] A. Sainz M., D. Mazzoni A., Aglietti E., Caballero A., (2004), Thermochemical stability of spinel ($MgO{\cdot}Al_2O_3$) under strong reducing conditions. *Mater. Chem. Phys*. 86: 399-408.

[5] Ping L. R., Azad A. M., Dung T. W., (2001), Magnesium aluminate ($MgAl_2O_4$) spinel produced via self-heat-sustained (SHS) technique. *Mater. Res. Bull.* 36: 1417–1430.

[6] Saha P., Mahajan R., Ganesh I., Srinivas B., Johnson R., (2004), Microwave assisted solid state reaction synthesis of $MgAl_2O_4$ spinel powders. *J. Euro. Ceram. Soc*. 24: 201–207.

[7] Singha V., Chakradharb R. P. S., Raoc J. L., Dong-Kuk K., (2007), Synthesis, characterization, photoluminescence and EPR investigations of Mn doped $MgAl_2O_4$ phosphors. *J. Solid State Chem*. 180: 2067–2074.

[8] Pati K., Pramanik P., (2000), Low-temperature chemical synthesis of nanocrystalline $MgAl_2O_4$ spinel powder. *J. Am. Ceram. Soc*. 83: 1822–1824.

[9] Sieber H., Hesse D., Panb X., Sen St., Heydenreich J., (1996), TEM investigations of spinel-forming solid state reactions: Reaction mechanism, film orientation, and interface structure during $MgAl_2O_4$, formation on MgO (001) and $A1_2O_3$, (11.2) single crystal substrates. *Z. Anorg. Allg. Chem*. 622: 1658-1666.

[10] Kim C.-H., Kwon I.-E., Park C.-H., Hwang Y.-J., Bae H.-S., Yu B.-Y., Pyun C.-H., Hong G.-Y., (2000), Intensive green emission of $ZnAl_2O_4$: $Mn^{2+}ZnAl_2O_4$: Mn^{2+} under vacuum ultraviolet and low voltage cathode ray excitation. *J. Alloys Comp*. 311: 33–39.

[11] Barros B. S., Melo P. S., Kiminami R. H. G. A., Costa A. C. F. M., de Sa G. F., Alves Jr. S., (2006), Photophysical properties of Eu^{3+} and Tb^{3+}doped $ZnAl_2O_4$ phosphors obtained by combustion reaction. *J. Mater Sci*. 41: 4744–4748.

[12] Lima S. A. M., Sigoli F. A., Davolos M. R., Jafelicci Jr M., (2002), Europium (III)-containing zinc oxide from Pechini method. *J. Alloys Comp.* 344: 280–284.

[13] Nakagawa H., Ebisu K., Zhang M., Kitaura M., (2003), Luminescence properties and afterglow in spinel crystals doped with trivalent Tb ions. *J. Lumin.* 102–103: 590–596.

[14] Jeong H., Kang M., (2010), Hydrogen production from butane steam reforming over Ni/Ag loaded $MgAl_2O_4$ catalyst. *Appl. Catal. B: Environ*. 95: 446-455.

[15] Evans O. R., Bell A. T., Tilley T. D., (2004), Oxidative dehydrogenation of propane over vanadia-based catalysts supported on high-surface-area mesoporous $MgAl_2O_4$. *J. Catal*. 226: 292-300.

[16] Li W. C., Comotti M., Lu A. H., Schuth F., (2006), Nanocast mesoporous $MgAl_2O_4$ spinel monoliths as support for highly active gold CO oxidation catalyst. *Chem. Commun*. 16: 1772-1774.

[17] Laobuthee A., Wongkasemjit S., Traversa E., Laine R. M., (2000), $MgAl_2O_4$ spinel powders from oxide one pot synthesis (OOPS) process for ceramic humidity sensors. *J. Eur. Ceram. Soc*. 20: 91–97.

[18] Ding Z., Zhang M., Han J., (2003), Synthesis of magnesium aluminate powders utilizing the solubility relationships in the Mg–Al–Oxalic acid–H_2O system. Harbin Institute of Technology, Harbin 150001. *China Bulg. J. Phys*. 30: 152–157.

[19] Fa-tang Li., Zhaoa Ye., Liua Y., Haoa Y-J., Liua R-H., Zhao D-Sh., (2011), Solution combustion synthesis and visible light-induced photocatalytic activity of mixed amorphous and crystalline $MgAl_2O_4$ nanopowders. *Chem. Eng. J*. 173: 750–759.

[20] Chena C. C., Lua C. S., Chungb Y. C., Jan J. L., (2007), UV light induced photodegradation of malachite green on TiO_2 nanoparticles. *J. Hazard. Mater*. 141: 520-528.

[21] Kusuma H. S., Sholihuddin R. I., Harsini M., Darmokoesoemo H., (2016), Electrochemical degradation of malachite green dye using Carbon/TiO_2 Electrodes. *J. Mater. Environ. Sci.* 7: 1454-1460.

[22] Hongwei M., Bis H. L., Davi D., Hsiu-wen wang H., Chipera Steve J., (2009), Determination of the crystal structure of sanderite, $MgSO_4{\cdot}2H_2O$, by X-ray powder diffraction and the charge flipping method. *Am. Mineral*. 94: 622–625.

[23] Young O. Se., Chan-Gyu Lee L., Shapiro Alexander J., Egelhoff William F., Vaudin Mark Jr. D., Jennifer Ruglovsky L., Mallett J, Pong W. T., Philip D., (2008), X-ray diffraction study of the optimization of MgO growth conditions for magnetic tunnel junctions. *J. Appl. Phys*. 103: 07A920.

[24] Djebaili K., Mekhalif Z., Boumaza A., Djelloul A., (2015), XPS, FTIR, EDX, and XRD analysis of Al_2O_3 scales grown on PM2000 Alloy. *J. Spec*ss. 16: 1-18.

[25] Plesingerova B., Stevulov N., Luxov M., Boldi E., Arov Z., (2000), Mechanochemical synthesis of magnesium aluminate spinel in oxide-hydroxide systems. *J. Mat. Syn. Proc.* 87: 2020-2024.

[26] Janitabar Darzi S., Mahjoub A. R., Bayat A., (2016), Synthesis and characterization of visible light active S-doped TiO_2 nanophotocatalyst. *Int. J. Nano Dimens.* 7: 33-40.

[27] Li S., Hu S., Zhang J., Jiang W., Liu J., (2017)., Facile synthesis of Fe(2)O(3) nanoparticles anchored on Bi(2)MoO(6) microflowers with improved visible light photocatalytic activity. *J. Colloid Interf. Sci*. 497: 93-101.

[28] Joachim K., Rajarshi R., Raju R., (2017), pH-responsive magnetic pickering. *Germany J. Colloid Interf. Sci*. 497: 93-101.

[29] Hosseinpour Z., Alemi A., Khandar A. A., Zhao X., Xie Y., (2015), A controlled solvothermal synthesis of CuS hierarchical structures and their natural-lightinduced photocatalytic properties. *New J. Chem.* 39: 5470-5746.

[30] Maria Magdalane C., Kaviyarasu K., Judith Vijaya J.,

Siddhardha B., Jeyaraj B., (2016), Photocatalytic activity of binarymetal oxide nanocomposites of CeO_2/CdO nanospheres: Investigation of optical and antimicrobial activity. *J. Photochem. Photobiol. B: Biology*. 163: 77-86.

[31] Tolia J. V., Chakraborty M., Murthy Z. V. P., (2012), Photocatalytic degradation of malachite green dye using doped and undoped ZnS nanoparticles. *Polish J. Chem. Technol.* 14: 16-21.

[32] Deepa N., Meghna P., Kandasamy S., (2014), Experimental studies on decolonisation of malachite dye using continuous photocatalytic reactor. *Int. Res. J. Env. Sci.* 3: 14-21.

[33] Hameed B. H., Lee T. W., (2009), Degradation of malachite green in aqueous solution by Fenton process. *J. Hazard. Mater.*164: 468-472.

[34] Abilarasu A., Somanathan T., Saravanan A., Saravanan V., Rajakumar P., (2016), Enhanced photocatalytic degradation of malachite green on spinel ferrite (Nickel/Magnesium Ferrite) under direct sun light. *Int. J. Pharma. Bio. Sci.* 7: 93-99.

[35] Harsini S. M., Darmokoesoemo H., (2016), Electrochemical degradation of malachite green dye using carbon/TiO_2 electrodes. *J. Mater. Environ. Sci*. 7: 1454-1460.

[36] Hu K. H., Meng M., (2013), Degradation of malachite green on MoS_2/TiO_2 nanocomposite. *Asian J. Chem*. 25: 5827-5829.

[37] Ameta K., Tak P., Soni D. S. C., (2014), Ameta, photocatalytic decomposition of malachite green over lead chromate powder. *Sci. Rev. Chem. Commun*. 4: 38-45.

[38] Bansal P., Bhullar N., Sud D., (2009), Studies on photodegradation of malachite green using TiO_2/ZnO photocatalyst. *Desalin. Water Treatment*. 12: 108-113.

[39] Sols-Casados D., Escobar-Alarcn L., Fernndez M., Valencia F., (2013), Malachite green degradation in simulated wastewater using Nix : TiO_2 thin films. *Fuel*. 110: 17-22.

[40] Soni H., Nirmal Kumar J. I., (2014), UV light induced photocatalytic degradation of malachite green on tio_2 nanoparticles. *Int. J. Recent. Res. Rev*. 7: 10-15.

[41] Khezami L., Taha K. K., Ghiloufi I., Mir L. E., (2016), Adsorption and photocatalytic degradation of malachite green by vanadium doped zinc oxide nanoparticles. *Water. Sci*. *Technol*. 73: 881-889.

[42] He H-Y., (2015), Photocatalytic degradations of malachite green on magnetically separable $Ni_{1-x}Co_xFe_2O_4$ nanoparticles synthesized by using a hydrothermal process. *Am. Chem. Sci. J*. 6: 58-68.

[43] Afshar S., Samari Jahromi H., Jafari N., Ahmadi Z., Hakamizadeh M., (2011), Degradation of malachite green oxalate by UV and visible lights irradiation using Pt/TiO_2/SiO_2 nanophotocatalyst. *Sci. Iran*. 18: 772-779.

[44] Asiltürk M., Sayılkan F., Arpaç E., (2009), Effect of Fe^{3+} ion doping to TiO_2 on the photocatalytic degradation of malachite green dye under UV and vis-irradiation. *J. Photochem. Photobiol*. *A: Chem*. 203: 64-71.

[45] Dutta D. P., Ramakrishnan M., Roy M., Kumar A., (2017), Effect of transition metal doping on the photocatalytic properties of $FeVO_4$ nanoparticles. *J. Photochem. Photobiol. A: Chem*. 335: 102-111.

[46] Zhou X., Zhang X., Feng X., Zhou J., Zhou S., (2016), Preparation of a La/N co-doped TiO_2 film electrode with visible light response and its photoelectrocatalytic activity on a Ni substrate. *Dyes & Pigm.* 125: 375-383.

[47] Modirshahla N., Behnajady M. A., (2006), Photooxidative degradation of malachite green (MG) by UV/H_2O_2: Influence of operational parameters and kinetic modeling. *Dyes & Pigm.* 70: 54-59.

[48] Ghaedi M., Mosallanejad N., (2014), Study of competitive adsorption of malachite green and sunset yellow dyes on cadmium hydroxide nanowires loaded on activated carbon. *J. Ind. Eng*. *Chem*. 25: 1085-1096.

[49] Ghaedi M., Ansari A., Habibi M. H., Asghari A. R., (2014), Removal of malachite green from aqueous solution by zinc oxide nanoparticle loaded on activated carbon: Kinetics and isotherm study. *J. Ind. Eng. Chem.* 20: 17-28.

[50] Mirzajani R., Ahmadi S., (2015), Melamine supported magnetic iron oxide nanoparticles (Fe_3O_4@Mel) for spectrophotometric determination of malachite green in water samples and fish tissues. *J. Ind. Eng. Chem*. 23: 171-178.

[51] Bojinova A. S., Carolina Papazova I., Irina Karadjova B., Ioannis P., (2008), Photocatalytic degradation of malachite green dyes with TiO_2/WO_3 composite. *Eur. J. Anal. Chem.* 3: 34-43.

[52] Elhalil A., Tounsadi H., Elmoubarki R., Mahjoubi F. Z., Farnane M., Sadiq M., Abdennouri M., Qourzal S., Bark N., (2016), Factorial experimental design for the optimization of catalytic degradation of malachite green dye in aqueous solution by Fenton process. *Water. Res. Indus*. 15: 41–48.

[53] Al-gubury H. Y., (2016), The effect of coupled titanium dioxide and cobalt oxide on photo catalytic degradation of malachite green. *Int. J. Chem. Tech. Res*. 9: 227-235.

[54] Kumar A., Rout L., Satish Kumar Achary L., Mohanty A., Marpally J., Chand P. K., Dash P., (2016), Design of binary SnO_2-CuO nanocomposite for efficient photocatalytic degradation of malachite green dye. *AIP Conf. Procs.* 1724: 020027-020078.

[55] Deepa N., Meghna P., Kandasamy S., (2014), Experimental studies on decolonization of malachite dye using continuous photocatalytic reactor. *Int. Res. Environ. Sci*. 3: 14-21.

[56] Shanthi S., Manjula R., Vinulakshmi M., Rathina Bala R., (2014), Studies on the photo degradation of malachite green dye by the synthesized ZnO nano particles with different sources of energy. *Int. J. Res. In Pharm. Chem.* 4: 571-576.

[57] Garg V. K., Kumar R., Gupta R., (2004), Removal of malachite green dye from aqueous solution by adsorption using agro-industry waste: A case study of Prosopis cineraria. *Dyes & Pigm.* 62: 1–10.

[58] Zhang H., Yang J., Ying Liu Y., Yan Song S., Li Liu X., Fang Ma J., (2016), Visible light photodegradation of organic dyes, reduction of Cr (VI) and catalytic oxidative desulfurization by a class of polyoxometalate-based inorganic-organic hybrid compounds. *Dyes & Pigm.* 133: 189-200.

[59] Tsvetkov M. P., Zaharias K. L., Cherkezova-Zheleva Z. P., Milanova M. M., Mitov I. G., (2015), Photocatalytic activity of nanostructure zinc ferrite-type catalysts in degradation of malachite green under UV-light. *Bulg. Chem. Communic*. 47: 354–359.

[60] Abilarasu A., Somanathan T., Saravanan1 A., Saravanan V., Rajakumar P., (2016), Enhanced photocatalytic degradation of malachite green on spinel ferrite (Nickel/ Magnesium Ferrite) under direct Sun light. *Int. J. Pharm. Bio. Sci*. 7: 93-99.

[61] Khademinia Sh., Behzad M., Kafi-Ahmadi L., Hadilou S., (2018), Hydrothermally synthesized strontium arsenate nanomaterial through response surface methodology. *Z. Anorg. Allg. Chem*. 644: 221–227.